Effect of fluctuations on the onset of density-driven convection in porous media

Michael Bestehorn and Abbas Firoozabadi

Citation: Phys. Fluids **24**, 114102 (2012); doi: 10.1063/1.4767467
View online: http://dx.doi.org/10.1063/1.4767467
View Table of Contents: http://pof.aip.org/resource/1/PHFLE6/v24/i11
Published by the American Institute of Physics.

Effect of fluctuations on the onset of density-driven convection in porous media

Michael Bestehorn[1,a)] and Abbas Firoozabadi[2,b)]
[1]*Department of Theoretical Physics, Brandenburg University of Technology, 03044 Cottbus, Germany*
[2]*Reservoir Engineering Research Institute (RERI), Palo Alto, California 94306, USA and Department of Chemical and Environmental Engineering, Yale University, New Haven, Connecticut 06511, USA*

(Received 27 February 2012; accepted 2 October 2012; published online 26 November 2012)

We study the dissolution of CO_2 in saline aquifers. The long diffusion times can be accelerated by orders of magnitude from mass transfer that origins from convection. Convection occurs at a critical time via a phase transition from the horizontally homogeneous diffusion state. To start the instability, perturbations that break the horizontal translation symmetry are necessary. We start with the basic equations and the boundary conditions, examine the linearized equations around the diffusive time and z-dependent base state and compare different definitions of the critical time found in the literature. Taking a simple model we show the role of fluctuations for delayed instabilities if the control parameter is slowly swept through the bifurcation point. Apart from the critical time we use a "visible" time where convection is manifested in the vertical CO_2 transport. We specify the perturbations with respect to their strength and length scale, and compute the critical times for various cases by numerical integration of the basic equations in two spatial dimensions. Fluctuating concentration at the upper boundary, fluctuating porosity as well fluctuating permeability are studied in detail. For the permeability fluctuation, the compressibility of the fluid becomes important and the velocity field cannot be derived from a stream function. Our work also includes non-isothermal conditions with a prescribed vertical geothermal gradient and space dependent thermal conductivity. Temperature fields for different standard configurations are computed numerically and serve as starting condition for density-driven convection. Based on our work, we conclude that the visible time is much larger than the critical time. The visible time is a strong function of strength and length scale of the perturbations.
[http://dx.doi.org/10.1063/1.4767467]

I. INTRODUCTION

Storage of carbon dioxide in saline aquifers in the subsurface is potentially the most promising option in reduction of this greenhouse gas in the atmosphere. Saline aquifers are spread throughout the world and have enormous capacity for storage.[1] Some of the aquifers offer the advantage of solubility trapping which may alleviate the concerns from CO_2 leakage to the environment. When CO_2 dissolves in water or in brine, the density may increase about one percent (by weight). The increase in density can result in convection currents that in some cases dramatically improve the rate of dissolution of CO_2. Without natural convection, the main mechanism of dissolution is through Fickian diffusion which is known to be slow.

The change from the purely diffusive process to the onset of convection and density-driven mixing can be considered as a non-equilibrium phase transition.[2] At a certain critical bifurcation

a)bes@physik.tu-cottbus.de.
b)abbas.firoozabadi@yale.edu.

point in parameter space, the old state becomes unstable and a new one becomes stable. To achieve this exchange of stability, there is a need for a driving force in form of fluctuations to leave the old state, both in nature and in computations. Without such forces, the system may stay in the unstable state for an unpredictable time.

The process of CO_2 dissolution starts first from Fickian diffusion without macroscopic fluxes that leads to a slowly growing, horizontally homogeneous diffusion layer under the upper boundary. As long as the diffusive layer does not exceed a critical thickness, the flux-less state is stable and fluctuations are damped in time. But when an adequate critical thickness of the dissolved layer is developed, the system passes the critical point and arbitrarily small disturbances may grow, giving way to a new convective state. These disturbances can be provided by inhomogeneous rock properties, inhomogeneous thermal gradients or fluctuations of the CO_2 concentration on the top of the domain by influence of the gas phase above.

A number of authors have studied density-driven mixing in the context of CO_2 sequestration in the subsurface.[3–9] All these authors point out to a critical time at which the critical thickness is reached and the mixing from CO_2 begins due to natural convection. Different approaches and methods have been used to compute the critical time. Some authors introduce perturbations at the boundary when CO_2 is assumed to be in local equilibrium with the water phase.[3–5,7] Others vary some of the rock properties in the domain.[7,8] In some works, the time when initial fluctuations start to grow is defined as critical.[4,6] As we will see in this work, often the result for the critical time is very different from one approach to another sometimes more than a factor of ten.

The critical time strongly depends on the kind and size of initial or persistent fluctuations of the material properties of the rocks and/or of boundary conditions (b.c.).

This work presents a comprehensive analysis of density-driven convection in porous media originating from various perturbations. We consider noise and fluctuations in porosity, permeability, and in the upper boundary conditions of the brine layer. Size and length scale of the perturbations are varied over a factor of 1000 (size) and 15 (length scale) and their influence on the critical time (after which convection occurs) is studied. We use the "one percent time" what we also call "visible time," i.e., the time where the deviation of the total CO_2 flux (convection and diffusion) through the upper interface is one percent larger than that by diffusion alone. This criterion can be found in previous works.[7] We examine permeability inhomogeneity systematically through the Dykstra-Parsons coefficient in a wide range.[10,11] Permeability inhomogeneity may be the most logical step in relation to density-driven mixing due to large variations even in the porous media that are believed to be homogeneous. We also examine the effect of temperature gradient on density driven mixing. There is vertical temperature gradient in all the subsurface formations. Sometimes horizontal temperature gradients are also observed due to thermal conductivity that varies in the horizontal directions. Whereas the vertical geothermal gradient is too low to cause a buoyancy driven instability of the water layer,[12] the horizontal gradient generates a convective fluid motion even if it is very small. Such a motion violates the horizontal homogeneity and may trigger the density-driven convection without any further perturbations. We compare such effects for several strengths of the horizontal gradient for certain rock formations with those from the material fluctuations studied in the previous parts.

This paper is structured along the following lines. In Sec. II, we introduce the basic equations, scalings, and boundary conditions together with the material parameters used in the following computations. Section III presents the numerical method and shows a typical run. A parameter set is given and used for all following computations throughout the paper. Our results can be easily re-scaled to other parameter sets belonging to different aquifer depths and given in Table I to be discussed later. In Sec. IV we study the linearized equations around the diffusive, time-dependent base state and compare different definitions of the critical time. Section V examines a simple model to show the role of fluctuations for delayed instabilities, when the control parameter is slowly swept through the critical point. In Sec. VI the special form of randomly generated perturbations (1d and 2d) is described. Section VII states the critical times found for the incompressible flow where porosity and upper boundary concentration are assumed to be fluctuating. Section VIII presents the same results for slightly compressible flows and a fluctuating permeability assumed to be lognormal distributed, which is very often the case in natural rocks.[10] In Sec. IX we assume non-isothermal conditions

with a prescribed vertical temperature gradient and given space dependent thermal conductivity. The stationary temperature fields for several configurations (line discontinuities, enclaves) are computed numerically and serve as starting condition for the density-driven convection. In Sec. X we compare our results with those from the literature and draw some conclusions in Sec. XI.

II. DEFINITION OF THE SYSTEM

We consider a porous medium in a confined rectangular geometry in two or three spatial dimensions (Fig. 1). The medium is characterized by its porosity n and its permeability K. The medium is also assumed to be isotropic, but since we wish to study the effect of fluctuations, we allow for spatially varying material properties according to

$$n = n_0(1 + \gamma(\vec{r}^*)), \qquad K = K_0(1 + \beta(\vec{r}^*)). \tag{1}$$

The functions γ and β are distributed randomly in space (for more details see Sec. VI below), their amplitudes are assumed to be small, $|\gamma|, |\beta| \ll 1$. In (1), $\vec{r}^*$ is the position vector. Dependent and independent variables with an asterisk bear a dimension. We note that we consider either a varying porosity or a varying permeability, hence we shall not assume any correlations between these two quantities.

A. Basic equations

The fluid inside the medium is a mixture of water and dissolved CO_2. Its volumetric flux $\vec{q}^*(\vec{r}^*, t^*)$ is described by Darcy's law[13]

$$\vec{q}^* = -\frac{K_0}{\mu}(1 + \beta)(\nabla P^* + g\rho^*\hat{e}_z). \tag{2}$$

The density $\rho^*(\vec{r}^*, t^*)$ is given by the continuity equation

$$n_0(1 + \gamma)\partial_{t^*}\rho^* + \nabla^* \cdot (\rho^* \vec{q}^*) = 0. \tag{3}$$

The mass fraction of the dissolved carbon dioxide $C^*(\vec{r}^*, t^*)$ can be computed from

$$n_0(1 + \gamma)\partial_{t^*}C^* + \vec{q}^* \cdot \nabla^* C^* = n_0 D(1 + \gamma)\Delta^* C^* + n_0 D\nabla^*\gamma \cdot \nabla^* C^*. \tag{4}$$

Here, P^* is the pressure field, μ is the viscosity of the fluid, g is the acceleration due to gravity, and $\hat{e}_z$ is the vertical normal vector. The effective diffusivity is denoted by D and defined as

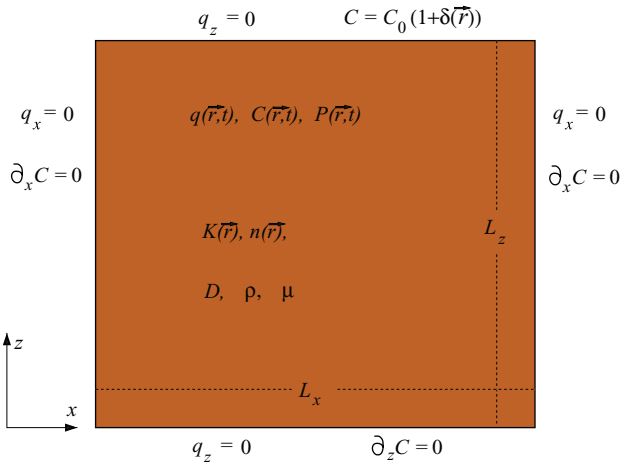

FIG. 1. Sketch of the system.

$D = D_m/(nF)$ with the molecular diffusion coefficient D_m of CO_2 in water and the formation factor F.[14] In the Boussinesq approximation, ρ^* depends linearly on C^* in (2) and (3) simplifies to the incompressibility condition $\nabla^* \cdot \vec{q}^* = 0$. For fluctuating permeability, compressibility should be taken into account as we shall discuss later. For this case we assume also in (3) a linear dependence of ρ^* on C^*, according to

$$\rho^* = \rho_0(1 + \alpha\, C^*) \tag{5}$$

with the coefficient

$$\alpha = \left.\frac{\partial \rho^*}{\partial C^*}\right|_{C^*=0}$$

and ρ_0 as the density of pure water. With (4) we find from (3)

$$\nabla^* \cdot \vec{q}^* = -\alpha D n_0 \left[(1+\gamma)\Delta^* C^* + \nabla^* \gamma \cdot \nabla^* C^*\right]. \tag{6}$$

The set (2) and (4)–(6) constitutes the basic equations for the variables $\vec{q}^*$, P^*, and C^* (or ρ^*). They are completed by no-flux boundary conditions on the domain walls

$$\begin{aligned} &x^* = 0,\ L_x: && q_x^* = 0, && \partial_{x^*} C^* = 0, \\ &z^* = 0: && q_z^* = 0, && \partial_{z^*} C^* = 0, \\ &z^* = L_z: && q_z^* = 0, && C^* = C_0(1 + \delta(\vec{r}^*)). \end{aligned} \tag{7}$$

As stated above, δ represents small fluctuations at the top boundary, which may originate from the dynamics in the gas layer above the liquid. If the water layer is in equilibrium with the pure CO_2 gas layer, C_0 is the saturation value which depends on temperature and pressure. This value as well as α of relation (5) can be computed using a generalized equation of state.[15]

B. Natural scaling

Scaling of all dependent and independent variables yields a system with the minimal number of independent dimensionless parameters. Work on convection traditionally is based on a Rayleigh number as most important control parameter. However, a Rayleigh number includes a length, normally the height or depth of the layer, which has a physical meaning only if the concentration gradient is established over the whole height. Due to the very long vertical diffusion time in aquifers that may have the height of more than 100 m, it is more appropriate to study a transient solution of a vertically invading concentration front of carbon dioxide from the top into water. Then the system can be considered as semi-infinite in depth at least in the early stage of its evolution and instead using a length, namely the total height, which is completely arbitrary in this case, we define

$$s = \frac{n_0 \mu D}{K_0 g \rho_0 \alpha C_0} \tag{8}$$

to scale all lengths and velocities of the system. This scale depends only on material properties. (Note that $s = L_z/R$ with R as the Rayleigh number, for cases where L_z plays a significant role.)

The appropriate time scale is that of the diffusion time with respect to s,

$$\tau = \frac{s^2}{D}, \tag{9}$$

the scaling of all other quantities is straightforward. We take

$$\vec{r}^* = s\,\vec{r}, \qquad t^* = \tau\, t, \tag{10}$$

$$\vec{q}^* = \vec{q}\,\frac{n_0 D}{s}, \quad C^* = C_0\, C, \quad P^* = P\,\frac{\mu n_0 D}{K_0}, \tag{11}$$

where all variables without an asterisk bear no dimension. Inserting these into the basic set yields a system of dimensionless equations,

$$\vec{q} = -(1+\beta)(\nabla \bar{P} + C\hat{e}_z), \tag{12}$$

$$(1+\gamma)\partial_t C + \vec{q}\cdot\nabla C = (1+\gamma)\Delta C + \nabla\gamma\cdot\nabla C, \tag{13}$$

$$\nabla\cdot\vec{q} = -\alpha C_0\left[(1+\gamma)\Delta C + \nabla\gamma\cdot\nabla C\right] \tag{14}$$

with

$$\bar{P} = P - P_{HS}$$

and $P_{HS} = -z/\alpha C_0$ as the hydrostatic pressure. The domain size is now transformed to

$$0 \le x \le x_1 = L_x/s, \qquad 0 \le z \le z_1 = L_z/s. \tag{15}$$

We note that these time and length scales are already used in Ref. 6.

C. Boussinesq approximation and homogeneous porous medium

For the sake of completeness we list the basic equations in the Boussinesq approximation[13,16] and for the case $\beta = \gamma = 0$:

$$\vec{q} = -\nabla\bar{P} - C\hat{e}_z, \tag{16}$$

$$\partial_t C = -\vec{q}\cdot\nabla C + \Delta C, \tag{17}$$

$$\nabla\cdot\vec{q} = 0. \tag{18}$$

In this formulation, there are no parameters.

D. Parameters

In this paper, we take

$$\alpha = 0.27,$$

a value found using the CPA (cubic-plus-association) equation of state.[15] For the porous media we assume

$$K_0 = 0.5\cdot 10^{-12}\ \mathrm{m}^2, \quad n_0 = 0.2.$$

The values for α, C_0, ρ_0, μ, and D depend on temperature and pressure, and therefore on the depth of the aquifer. Some values can be found in Table I. If we specify quantities with a dimension, we take the values of the first row for 50 bars and 30 °C. For these values, the scales read

$$s \approx 6\cdot 10^{-3}\ \mathrm{m}, \qquad \tau \approx 17\cdot 10^{3}\ \mathrm{s} \approx 0.2\ \mathrm{day}.$$

TABLE I. Parameters and scales for three values of temperature and pressure. The values for C_0 are from Ref. 15, for D from Ref. 18, for μ and ρ_0 from Ref. 17.

Temperature (°C)	Pressure (bar)	$D\times 10^{-9}$(m^2/s)	$\mu\times 10^{-4}$ (Pa s)	ρ_0 (kg/m^3)	C_0	s (m)	τ (s)
30	50	2.15	8.0	998	0.043	0.0060	17 000
40	75	2.7	6.5	995	0.048	0.0055	11 000
50	100	3.4	5.6	992	0.049	0.0059	10 000

III. NUMERICAL METHOD AND NONLINEAR RESULTS

A. Method

We briefly introduce the numerical method applied for the full nonlinear problem. We restrict to the case of an incompressible flow and the Boussinesq approximation. If the system is considered in 2D (x, z), the volumetric flux can be represented by a stream function

$$q_x = \partial_z \Phi(x, z, t), \qquad q_z = -\partial_x \Phi(x, z, t), \tag{19}$$

which satisfies (18). Here, we assume $\beta = 0$ (the case of fluctuating permeability will be discussed separately). The pressure can be eliminated from (16) by forming twice the curl. The system to be solved numerically then takes the form

$$\Delta \Phi = \partial_x C, \tag{20}$$

$$(1+\gamma)\partial_t C + \partial_z \Phi \partial_x C - \partial_x \Phi \partial_z C = (1+\gamma)\Delta C + \nabla \gamma \cdot \nabla C. \tag{21}$$

Equation (21) is discretized by finite differences on an $M \times N$ mesh. Spatial derivatives are expressed by centered space schemes, for time iteration we used an explicit Euler forward method.[19] The convective terms are computed by a conservative upwind scheme, also called donor cell method.[20,21] To determine Φ, the Laplacian in (20) is inverted. In horizontal direction, we use a sine-transform[22]

$$\Phi(x, z) = \sum_n^M \varphi_n(z) \sin\left(\frac{\pi n}{x_1} x\right), \qquad \partial_x C(x, z) = \sum_n^M c_n(z) \sin\left(\frac{\pi n}{x_1} x\right)$$

fulfilling the b.c. (7). Instead of (20), this yields a set of M decoupled ordinary differential equations of the form

$$\left(d_z^2 - \frac{\pi^2 n^2}{x_1^2}\right) \varphi_n = c_n, \qquad n = 1 \ldots M. \tag{22}$$

After discretization of z, one inverts M tridiagonal systems of length N at each time step achieved by a standard routine (e.g., Thomas algorithm, see Ref. 23).

The method is an extension of the semi-implicit pseudo-spectral scheme developed and used earlier in Ref. 24, where details on accuracy and convergence are presented.

B. A typical run

Figure 2 shows a time series with the specified parameters in Sec. II D. We set $\delta = 0$ and allow for an inhomogeneous white noise fluctuation in space for n with $|\gamma| < 0.01$. The integration domain is 20 m $\times$ 20 m which is resolved by a mesh with 512 $\times$ 2500 points. The linearly fastest growing mode has a wavelength of about 0.4–0.8 m (see Fig. 3 below), thus the critical modes are resolved with 10–20 mesh points which is a reasonable compromise between accuracy and effort. In the vertical direction, the early fingers are also resolved with more than 10 mesh points.

In the figure, only the upper 10% of the layer is shown. With this resolution, the time step could be as large as 0.4 ($\approx$ 0.08 days) to achieve convergence.

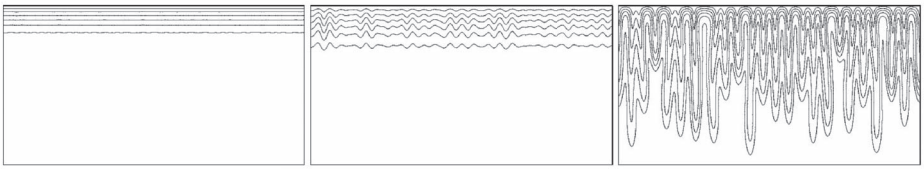

(a) (b) (c)

FIG. 2. Onset of instability and early finger formation. The layer has a width of 20 m. The plotted area has a height of 2 m, scaling in the vertical is enlarged by a factor 5. (a) 150 days, (b) 330 days, and (c) 750 days.

The typical scenario can be divided into four regions:

1. Early phase (Fig. 2(a)): 1D diffusion front. The CO_2 diffuses slowly into the water layer from the top, homogeneously in the x direction. Small perturbations caused by γ are damped.
2. Instability (Fig. 2(b)): The diffusion front becomes unstable when it reaches a certain thickness. Then the perturbations can grow in the form of periodic waves. The wave vector of these waves correspond roughly to the one with the largest linear growth rate (see Sec. IV).
3. Finger formation (Fig. 2(c)): When the amplitude of the perturbation reaches a certain magnitude, nonlinear effects become important. Fingers of high concentration are formed and fall down rapidly. The fluid moves now macroscopically and rather thin areas of saturated water are formed due to upwelling liquid. This increases the mean concentration gradient near the surface strongly and as a consequence the CO_2 mass flux through the upper boundary is increased as well. The width of the finger is already much larger than the wavelength of the patterns at onset. This coarsening process is also known from the classical Rayleigh-Taylor instability[25] and continues to the long-time limit.
4. Saturation (not shown): At very late times the fingers lose their shapes, merge and disappear. Finally, the whole water layer is homogeneously saturated and the fluid motion comes to an end.

IV. THE LINEAR PROBLEM

A. Base state

In this section we neglect all fluctuations and use the Boussinesq-set (16)–(18). If we take $C(t=0)=0$, $\vec{q}(t=0)=0$ as initial condition, the process is purely diffusive in the beginning. If the layer is deep enough there is no effect of the lower boundary for times much shorter than the vertical diffusion time L_z^2/D, and the system can be considered as semi-infinite. The exact solution of the diffusion equation (17) reads

$$C^0(z,t) = 1 - \mathrm{erf}\left(\frac{z_1 - z}{2\sqrt{t}}\right), \tag{23}$$

where erf denotes the error function.[26] This corresponds to a one-dimensional CO_2 saturated layer that invades from the top. Since the saturated layer is heavier than pure water, this layer may get unstable due to buoyancy after it reaches a certain thickness. Since the base state is time dependent, the stability analysis is subtle and the definition of the critical point (critical depth of the diffusive layer) is not unique in the literature. We shall come back to this point later.

With the normal mode representation

$$\Phi(x,z,t) = \Phi_k(z,t)\,\mathrm{e}^{ikx}, \qquad C(x,z,t) = C^0(z,t) + C_k(z,t)\,\mathrm{e}^{ikx}, \tag{24}$$

(20) and (21) turn after linearization into the system

$$\left(\partial_{zz}^2 - k^2\right)\Phi_k = ikC_k, \tag{25}$$

$$\partial_t C_k = ik\Phi\partial_z C^0 + \left(\partial_{zz}^2 - k^2\right)C_k \tag{26}$$

with

$$\partial_z C^0 = \frac{1}{\sqrt{\pi t}}\mathrm{e}^{-\frac{(z-z_1)^2}{4t}} \equiv g(z,t), \tag{27}$$

a normalized Gaussian.

From (25) and (26) one can derive a closed equation for C_k

$$\partial_t C_k = \hat{L}(z)C_k - k^2 g(z,t)\hat{L}(z)^{-1}C_k \tag{28}$$

with the differential operator

$$\hat{L}(z) = \partial_{zz}^2 - k^2 \tag{29}$$

and $\hat{L}^{-1}$ its inverse.

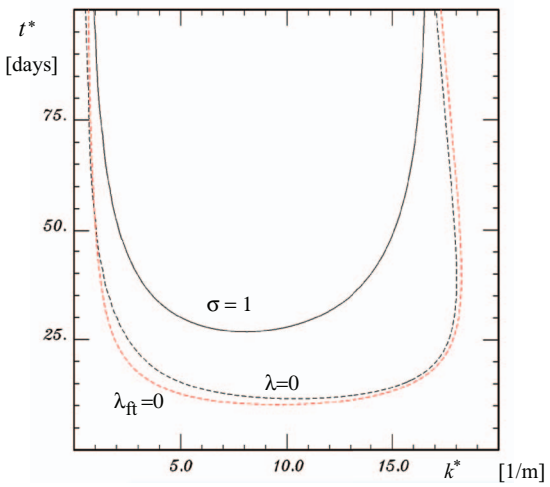

FIG. 3. Amplification factor, zero growth rate (dashed), and frozen time instability (red dashed).

To solve the linear problem with time dependent coefficients (28), the variable z is discretized on a grid with N points. The discretized version of (28) can be cast into the form

$$d_t \vec{u}_k(t) = \underline{M}(t, k^2)\, \vec{u}_k(t), \tag{30}$$

where the N elements of $\vec{u}_k$ are the mesh points of C,

$$(u_k(t))_i = C_k(z_i, t), \qquad z_i = \frac{i}{N}\, z_1 \tag{31}$$

and $\underline{M}$ is a $N \times N$ matrix with time dependent coefficients.

Following Ref. 4, we define the propagator $\underline{P}(t, t_0, k^2)$, a time dependent matrix that transforms the vector $\vec{u}_k(t_0)$ (e.g., the initial condition) to $\vec{u}_k(t)$, according to

$$\vec{u}_k(t) = \underline{P}(t, t_0, k^2)\, \vec{u}_k(t_0). \tag{32}$$

Inserting (32) into (30) yields a matrix differential equation

$$d_t \underline{P}(t, t_0, k^2) = \underline{M}(t, k^2)\, \underline{P}(t, t_0, k^2) \tag{33}$$

with initial condition

$$\underline{P}(t_0, t_0, k^2) = \underline{1}. \tag{34}$$

We use (32) to introduce an amplification factor

$$\sigma_k(t) = \rho(P(t, t_0, k^2)) \tag{35}$$

as the spectral radius (or the absolute value of the largest eigenvalue) of $\underline{P}$. The fastest growing mode has the direction of the eigenvector $\vec{p}_{\mathrm{m}}$ of $\underline{P}$ which belongs to the largest eigenvalue. For this mode, the relation

$$|\vec{p}_{\mathrm{m}}(t, k^2)| = \sigma_k(t) |\vec{p}_{\mathrm{m}}(t_0, k^2)| \tag{36}$$

holds. From (36), a temporary growth rate according to

$$\lambda_k(t) = \frac{\dot{\sigma}_k(t)}{\sigma_k(t)} \tag{37}$$

can be derived.

B. Numerical results

To find the spectral radius (35), the set (33) is solved numerically by an explicit fourth-order Runge-Kutta method[23] with the initial conditions (34). For discretization in z a mesh with $N = 200$ points is used. The system is not solved in the whole vertical domain $0 \le z \le z_1$ but only in the upper 10%, giving a high spatial resolution. The procedure is checked for convergence with respect to time step, spatial step size and size of integration domain.

Figure 3 shows the line where $\sigma_k = 1$ together with the line for the minimum of σ_k in the k–t plane for the parameters listed in Sec. II D. The line $\sigma_k(t) = 1$ denotes the time where the fastest growing initial perturbation has reached its initial amplitude. This could be one definition of the critical time. An alternative one is the minimum of σ_k which would coincide with a vanishing temporary growth rate (37).

C. Frozen-time analysis

Some authors employ the so-called frozen-time approach, also known as quasi-steady-state approximation,[27,28] which means that the time dependent coefficients of the differential equations are assumed constant and time is merely regarded as an external parameter. We compare the results of Sec. IV A with the frozen-time method and rewrite (30) as

$$d_t \vec{u}_k(t) = \underline{M}(T, k^2)\, \vec{u}_k(t), \tag{38}$$

where T denotes the frozen time. Equation (38) is standard and can be solved by

$$\vec{u}_k(t) = \vec{u}_k(0)\ \exp(\lambda_{\mathrm{ft}} t)$$

with

$$\lambda_{\mathrm{ft}} = \lambda_{\mathrm{ft}}(k^2, T)$$

as eigenvalues of $\underline{M}$. Onset of instability of the base state is then defined as the line in k–t-space where the largest eigenvalue has a vanishing real part. The lower dashed line in Fig. 3 shows this location and it can be seen that it almost coincides with the line of minimal amplification factor found from the non-modal analysis.

D. Discussion of results

From Fig. 3, it turns out that the critical time may vary between about 10 days and 30 days, depending on its definition. However, the size of the deviations from the diffusive state when σ exceeds a value of one is arbitrary as far as it is not clear how large the initial perturbations were. If we consider Fig. 2, it is clear that even after a much longer time of 150 days the concentration is still almost completely diffusive. Only after 330 days a significant wavy structure becomes visible. So it seems questionable if the linear criteria are useful at all in defining an onset time. In Ref. 6, the time where the spatial average of $C - C^0$ starts to increase is defined as critical time, because then disturbances grow. It is shown that this corresponds to the situation where the largest eigenvalue of $\underline{M} + \underline{M}^+$ with $\underline{M}$ from (38) and $\underline{M}^+$ its transpose is zero. However, the critical time based on this criterion differs only very little from that found by the frozen-time method. This is not surprising because $\underline{M}$ is almost symmetrical.

V. DYNAMIC CONTROL PARAMETER AND DELAYED BIFURCATION

The instability in the system under consideration has two time scales: one is provided by the time-dependent base state (23), the other by the growth rate of unstable modes of (28) when the base state has evolved to a certain critical thickness. The choice of initial conditions of the perturbations and fluctuations of several properties complicate the situation further. Since we wish to elucidate the interplay of these ingredients more general and apart from pure numerical results of the base system (12)–(14), we resort in this section to the most simple normal form showing a forward bifurcation

with fluctuations,

$$d_t\xi = \varepsilon\,\xi - \xi^3 + f(t). \tag{39}$$

Here, $\xi(t)$ denotes an order parameter, i.e., the amplitude of a certain spatial mode, etc., ε is the control parameter, $f(t)$ a delta-correlated fluctuation with

$$\langle f(t)\rangle = 0, \qquad \langle f(t)f(t')\rangle = Q\,\delta(t-t') \tag{40}$$

and $\langle ...\rangle$ the mean over different realizations of the fluctuations. Equation (39) describes a pitch fork bifurcation that takes place at $\varepsilon = 0$. For positive ε, the state $\xi = 0$ becomes unstable and in the long time limit the system tends to one of the two steady states $\xi_s = \pm\sqrt{\varepsilon}$, as long as fluctuations are small against $|\xi_s|$.

However, our system is more complicated due to the fact that for early times, $\xi = 0$ is stable (the diffusive state), as for larger times it becomes unstable and gives way to flow patterns (fingers). This can be modeled with (39), assuming a time dependent control parameter, which is taken in its most simple, linear form

$$\varepsilon(t) = a + v\,t \tag{41}$$

with $a < 0,\ \ v > 0$. The control parameter is swept through the critical point with the constant velocity v.

In the following we are only interested in the behavior near threshold and neglect the nonlinearity in (39). Further, time and ξ can be scaled so that $a = -1$ and only one relevant parameter, namely v, remains. The system we shall study now as a showcase reads

$$d_t\xi = (-1 + v\,t)\,\xi + f(t). \tag{42}$$

We show the effects of a dynamic control parameter, initial conditions, and internal fluctuations on a delayed bifurcation from the model (42).

A. Instability induced by an initial value

We start with the deterministic case $f = 0$. The solution to (42) reads

$$\xi(t) = G(t)\,\xi(0) \tag{43}$$

with the initial condition $\xi(0)$ at $t = 0$ and the Green's function

$$G(t) = \exp(-t + \frac{1}{2}v\,t^2). \tag{44}$$

A frozen-time analysis of (42) yields from $\varepsilon(t_c) = 0$ the critical time from where on any disturbance may grow as

$$t_c = \frac{1}{v}. \tag{45}$$

The amplification factor introduced in Sec. IV A would correspond to $G(t)$, the time t_1 where it is equal to one is found

$$t_1 = \frac{2}{v}, \tag{46}$$

just two times t_c. Starting with any finite (but small) perturbation $\xi(0)$, the system "accumulates" stability during the time while $\varepsilon < 0$.[29] Due to the constant sweep velocity v, it takes the same time after t_c until the perturbation reaches its initial size at t_1, see Fig. 4. This situation can be compared to our case if an initial perturbation in the form of a concentration field is given.

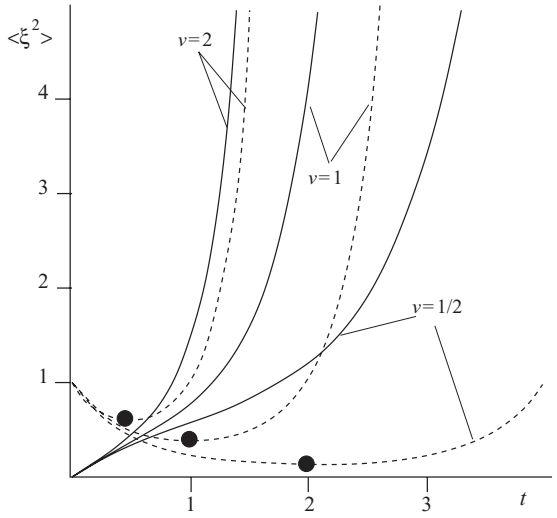

FIG. 4. Mean square of the order parameter with noise ($Q = 1$, solid) and without noise ($\xi(0) = 1$, dashed) for different sweep velocities. Critical times found by frozen-time analysis are at the minimum of the dashed lines (solid circles).

B. Noise induced instability

If noise is added, it is no longer necessary to start the instability by a non-zero initial condition.[30] The solution of (42) with $\xi(0) = 0$ reads

$$\xi(t) = \int_0^t dt'\; G(t-t')\, f(t'). \tag{47}$$

The mean square can be computed by the help of (40) according to

$$\langle \xi^2(t) \rangle \;= \frac{1}{2}\sqrt{\frac{\pi}{v}}\, Q \exp\left(\frac{(vt-1)^2}{v}\right)\left[\operatorname{erf}\left(\frac{vt-1}{\sqrt{v}}\right) + \operatorname{erf}\left(\frac{1}{\sqrt{v}}\right)\right]. \tag{48}$$

Although the size of ξ depends now on the strength of the noise Q, it is clear from Fig. 4 that the noise induced instability is delayed and again shows up mainly after about the double time that would be expected by the frozen-time approach.

For both cases of this simple example the difference between t_c and t_1 is of the size $1/v$ and can therefore become considerably large if v is small.

VI. RANDOM PERTURBATIONS

Perturbations are necessary to start the instability. In a real system, they can have different origins and therefore may differ in amplitude and length scale. One of the first numerical studies of convection in strongly inhomogeneous media can be found in Ref. 31 where the so-called turning bands method[32] is applied to create a porosity distributions having well-defined correlation lengths. For more recent work on fractal based models and further references see Ref. 33. In Ref. 8, random Fourier modes are weighted with a spectral density of Lorentzian shape leading also to a fluctuating quantity with a tunable correlation length in real space. In this paper we use a modified method of Ref. 8 as described in the following.

A. One dimension

Let $\eta(x)$ be a randomly varying function with zero mean in the interval $0 \le x \le x_1$,

$$\int_0^{x_1} \eta(x)\, dx = 0 \tag{49}$$

and normalized to

$$\frac{1}{x_1}\int_0^{x_1}\eta^2(x)\,dx = 1. \tag{50}$$

With the autocorrelation function

$$K(x) = \frac{1}{x_1}\int_0^{x_1}\eta(x')\eta(x'+x)\,dx' \tag{51}$$

one defines a correlation length

$$\ell = 2\int_0^{x_1} K^2(x)\,dx. \tag{52}$$

This definition is straightforward if we assume $K(x) = \exp(-x/\ell)$ and $\ell \ll x_1$.[34] Let η be represented by the finite sum

$$\eta(x) = \frac{1}{\sqrt{M_0}}\sum_{\substack{n=-M_0/2\\ n\neq 0}}^{M_0/2} e^{ik_n x}e^{i\varphi_n}, \qquad k_n = \frac{2\pi}{x_1}n, \quad \varphi_n = -\varphi_{-n} \tag{53}$$

with φ uniformly random-distributed in the interval $[0, 2\pi]$. From (51) and (52) one finds the relation $\ell = 2x_1/M_0$. If a random initial distribution with correlation length ℓ is desired, we may use the expression (53) with

$$M_0 = \frac{2x_1}{\ell}. \tag{54}$$

Using the central limit theorem it is shown that $\eta(x)$ is normally distributed with the variance $\langle\eta^2\rangle = 1$ if $M_0 \to \infty$, corresponding to the Gaussian white noise. We have examined the distribution of η for finite M_0 by a standard chi-squared test[35] and find good agreement with the Gaussian even for rather small $M_0 > 25$.

B. Two dimensions

The randomly distributed function $\eta(x, y)$ can be represented in 2D by

$$\eta(x,y) = \frac{1}{\sqrt{M_0N_0}}\sum_{\substack{m=-M_0/2\\ m\neq 0}}^{M_0/2}\sum_{\substack{n=-N_0/2\\ n\neq 0}}^{N_0/2} e^{i(k_m x+k_n y)}e^{i\varphi_{mn}},$$
$$k_m = \frac{2\pi}{x_1}m, \quad k_n = \frac{2\pi}{y_1}n, \quad \varphi_{mn} = -\varphi_{-m,-n} \tag{55}$$

and, if the distribution is assumed to be isotropic,

$$M_0 = \frac{2x_1}{\ell}, \qquad N_0 = \frac{2y_1}{\ell}. \tag{56}$$

Figure 5 shows 2D-patterns produced with (55) for three different correlation lengths.

VII. NUMERICAL RESULTS, INCOMPRESSIBLE CASE

Using the randomly distributed function η defined in Sec. VI, we present numerical solutions of the system (20) and (21) with the method described in Sec. III. Two global quantities are monitored as a function of time. One is the quantity

$$\bar{C}(t) = \frac{1}{V}\int_V d^3\vec{r}\; C(\vec{r}, t), \tag{57}$$

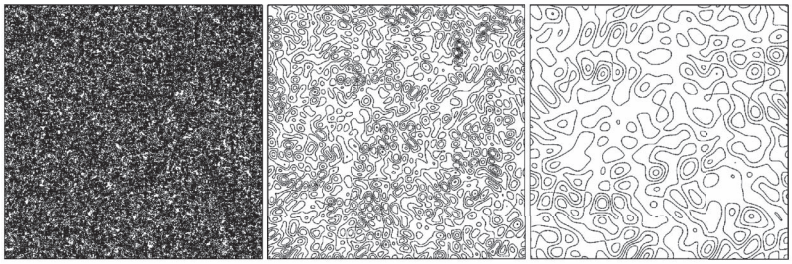

FIG. 5. Random dot patterns with different correlation lengths ℓ, side length of the frames is $x_1 = y_1 = 1$.

which is equal to one if total saturation is achieved (V denotes the total volume). The mass of dissolved CO_2 then corresponds to

$$M_{CO_2}(t) = M_{H_2O}\, C_0\, \bar{C}(t) + O(C^2). \tag{58}$$

The other one is the relative difference of the total mass flux j_{tot} (convective and diffusive) through the upper surface A to that of the purely diffusive flux $j_{diff} \sim 1/\sqrt{\pi t}$:

$$\Delta S(t) = \frac{1}{A}\int_A \frac{j_{tot} - j_{diff}}{j_{diff}} d^2 f = \frac{\sqrt{\pi t}}{A}\int_A \partial_z C d^2 f - 1, \tag{59}$$

where d^2f is the element of surface. If there is no convection, ΔS should vanish, up to numerical errors. In thermal convection, an analogue quantity is defined (convective over conductive heat flux) and called Nusselt number.[36] In the following we shall call ΔS the *convection number*.

A. Internal fluctuations

We first study the behavior of the convection number for different realizations of fluctuations γ of porosity n. Therefore we take

$$\gamma(x, z) = F\, \eta(x, z) \tag{60}$$

with η from (55). We can vary the two parameters ℓ and F. Figure 6 shows ΔS for three different values of this pair. It can be seen clearly that the time where convection starts to dominate depends strongly on both correlation length and amplitude of the perturbations.

In Fig. 7 we present a more systematic investigation in the plane spanned by ℓ and F. For each parameter pair we compute the time necessary for ΔS to reach 0.01. This corresponds to the situation where the magnitude of the total (convective and diffusive) flux is one percent of the diffusive flux. Then, contour lines are plotted for five runs with different random distribution of the phases φ_{mn} of (55) (thin lines). The bold lines show the average over the five runs.

Figure 7 reveals that there exists a certain optimal correlation length ℓ_c of the random distribution which leads to the fastest growing perturbation. This optimal length can be related to a critical wave number $k_c = 2\pi/\ell_c$ (wave number of the fastest growing mode) and compared to the linear computations and Fig. 3. It is interesting to see that the optimal correlation length seems to increase with decreasing amplitude F.

B. External fluctuations

1. Numerical results

Next we assume a homogeneous porosity ($\gamma = 0$) and examine the influence of concentration perturbations on the top boundary, $\delta \neq 0$ in (7),

$$\delta(x) = F\, \eta(x) \tag{61}$$

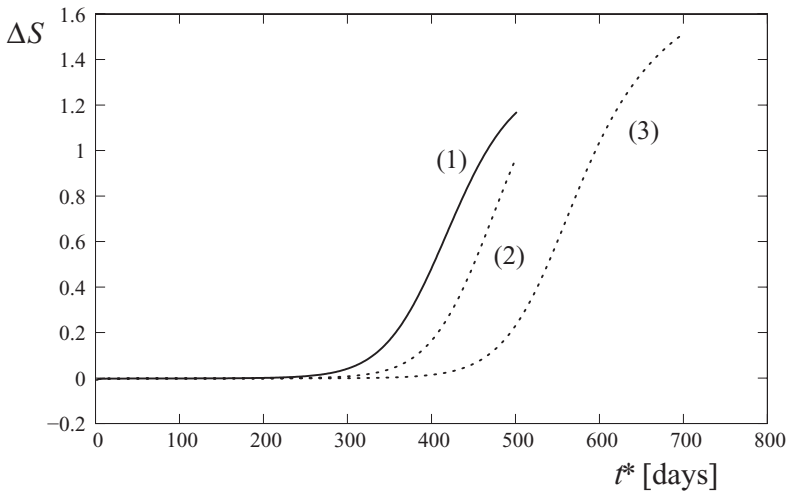

FIG. 6. Convection number ΔS according to (59) for three different pairs of (F, ℓ): (1) (0.003, 0.5 m), (2) (0.003, 0.1 m), (3) (0.0003, 0.5 m). The main influence comes from the size of perturbations, but also the length scale is important.

with η from (53). Figure 8 shows the dependence of the dynamics on amplitude and correlation length of δ. The result is qualitatively similar to that of fluctuating porosity, however, instability occurs a bit earlier for the same magnitude of F for the case of external fluctuations. Figure 9 shows again the one percent times in the parameter plane for five runs and their average. The differences between the single runs are much less pronounced than in Fig. 7 which may be due to the fact that the perturbations diffuse now from the top into the layer, which leads already to a kind of averaging in each particular run. The optimal correlation length is smaller now and the shift to larger values with decreasing amplitude is more pronounced.

2. *Diffusion of a random perturbation*

So far all computations are performed in 2D. Considering the linear problem this should be sufficient since (28) has exactly the same form in 2D and in 3D. However the "visible" one percent time depends on the size of the fluctuations available to trigger instability. The fluctuations are needed in the bulk. If they enter only via the boundary conditions for C at $z = z_1$, we have to study

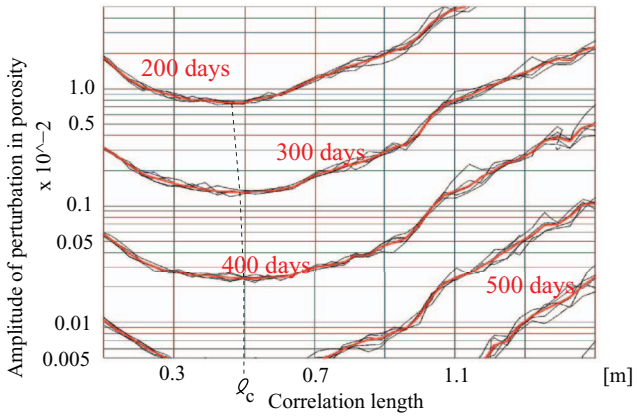

FIG. 7. Times necessary for the convection number ΔS to reach 0.01. There is an optimal correlation length ℓ_c of about 0.5 m, leading to the earliest possible onset time (dashed line is a guide to the eye).

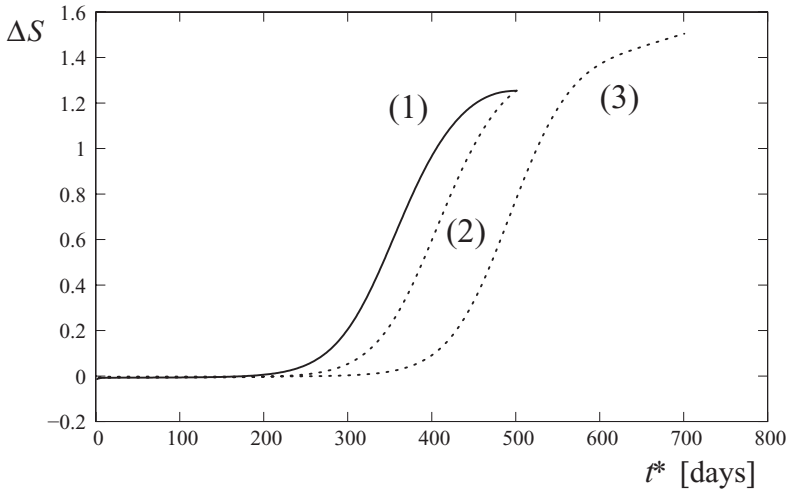

FIG. 8. ΔS for three different pairs of (F, ℓ): (1) (0.003, 0.5 m), (2) (0.003, 0.1 m), (3) (0.0003, 0.5 m), for fluctuations in C at the top of the layer.

the propagation of these randomly distributed perturbations from the surface into the bulk *before* convection starts, i.e., if the process is solely determined by diffusion. It will turn out that the rate of damping of the concentration perturbations through the medium depends on the dimensionality of space and is larger in 3D than in 2D. Before convection sets in, we find a solution of the diffusion equation

$$\partial_t C(x, z, t) = \Delta C(x, z, t). \tag{62}$$

To this end we consider a finite height z_1. The boundary conditions read

$$\partial_z C|_{z=0} = 0, \qquad C|_{z=z_1} = 1 + \xi(x, y) \tag{63}$$

and periodic in xy with the periodicity length x_1. The initial condition is

$$C(t = 0) = 0, \qquad \text{for} \quad z < z_1. \tag{64}$$

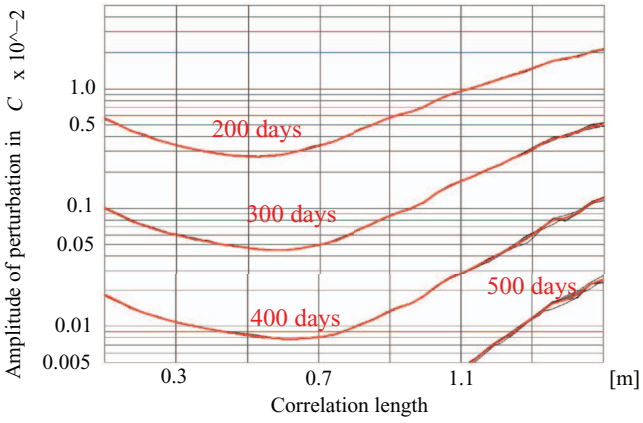

FIG. 9. One percent time, same as Fig. 7 but for fluctuations in C.

We first consider only one horizontal dimension x and the vertical dimension z. The perturbations are of the form (53) and a solution of (62) with (63) and (64) reads

$$C(x,z,t) = \sum_{m=-M_0/2}^{M_0/2} a_m C_m(z,t) \mathrm{e}^{ik_m x}, \qquad k_m = \frac{2\pi}{x_1} m \tag{65}$$

with

$$C_m(z,t) = \frac{\cosh k_m z}{\cosh k_m} + 2\sum_{n=0}^{N} (-1)^{n+1}\, \mathrm{e}^{-\lambda_{nm} t}\, \frac{\chi_n}{\lambda_{nm}} \cos \chi_n z \tag{66}$$

and

$$a_m = \begin{cases} \dfrac{1}{\sqrt{M_0}}\, \mathrm{e}^{i\varphi_m} & m \neq 0 \\ 1 & m = 0 \end{cases},$$

$$\chi_n = \frac{\pi}{2z_1}(1+2n), \qquad \lambda_{nm} = \chi_n^2 + k_m^2.$$

Again N is finite due to discretization of z.

To see how the initial perturbations at the interface penetrate into the bulk, we evaluate the standard deviation $\sigma(z,t)$ according to

$$\sigma^2(z,t) \;=\; \langle C^2 \rangle_x - \langle C \rangle_x^2. \tag{67}$$

Inserting (65) yields

$$\sigma^2(z,t) = \frac{1}{M_0} \sum_{\substack{m=-M_0/2 \\ m\neq 0}}^{M_0/2} C_m^2(z,t). \tag{68}$$

In Fig. 10, we have evaluated (68) for several times and the dimensionalized height $L_z = 20$ m.

In three dimensions, the solution of (62) takes the form

$$C(x,y,z,t) = \sum_{m,\ell=-M_0/2}^{M_0/2} a_{m\ell} C_{m\ell}(z,t) \mathrm{e}^{i(k_m x + k_\ell y)} \tag{69}$$

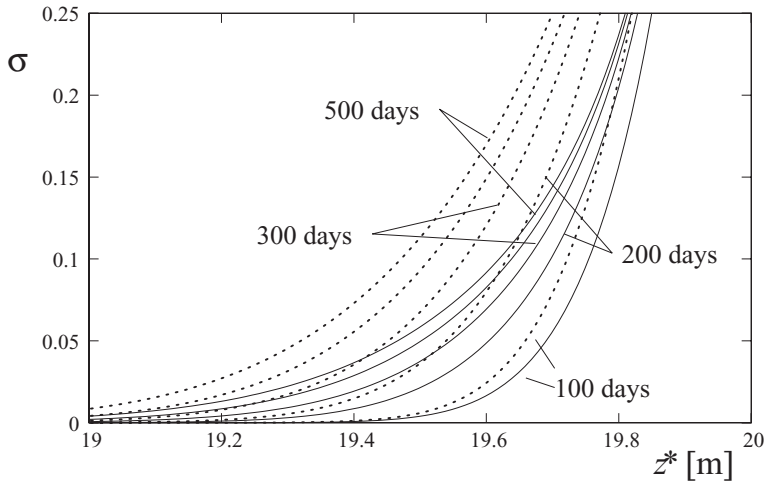

FIG. 10. Standard deviation of C at several times, dashed lines for 2D diffusion, solid for 3D. Parameters are $M_0 = 80$, $M = 200$.

with

$$C_{m\ell}(z,t) = \frac{\cosh k_{m\ell} z}{\cosh k_{m\ell}} + 2\sum_{n=0}^{N}(-1)^{n+1}\, \mathrm{e}^{-\lambda_{nm\ell} t}\, \frac{\chi_n}{\lambda_{nm\ell}} \cos \chi_n z \tag{70}$$

and

$$a_{m\ell} = \begin{cases} \dfrac{1}{M_0}\, \mathrm{e}^{i\varphi_{m\ell}} & m \neq 0 \text{ or } \ell \neq 0 \\ 1 & m = \ell = 0 \end{cases},$$

$$k_{m\ell} = \sqrt{k_m^2 + k_\ell^2}, \qquad \lambda_{nm\ell} = \chi_n^2 + k_m^2 + k_\ell^2.$$

Computing the standard deviation, one finds

$$\sigma^2(z,t) = \langle C^2\rangle_{xy} - \langle C\rangle_{xy}^2 = \frac{1}{M_0^2} \sum_{\substack{m,\ell=-M_0/2 \\ m=\ell\neq 0}}^{M_0/2} C_{m\ell}^2(z,t) \tag{71}$$

which is also plotted in Fig. 10 for the parameters of the 2D case. It is obvious that the perturbations propagate which much less damping in 2D than in 3D. The onset time t_c defined from the linearized problem is independent from spatial dimension, however, the amplitude of the perturbations still available at onset time is much smaller in 3D. This is due to the uniform distribution of the perturbations onto all available Fourier modes from $1 \ldots M_0$. In 2D the density of modes in Fourier space is constant, in 3D it is $\sim |\vec{k}|$. Therefore a larger part of the perturbations fall on small wavelengths. Small wavelengths are damped stronger than longer ones by diffusion on their way into the bulk until they can linearly grow, leading to a smaller perturbation available at $t = t_c$.

The amplitude decay of the perturbation depends also on the number of Fourier modes M_0 which take part on the random boundary condition, and therefore on the correlation length of the distribution, as defined in (54). Increasing M_0 leads to a larger number of short wave perturbations which are damped strongly while penetrating into the bulk. As a consequence, onset should occur later if M_0 is increased (or ℓ is decreased), in accordance with the findings of Sec. VII B 1 (Fig. 9).

We note that the size of N is not crucial, since the sums in (66) and (70) converge for $N \to \infty$. N should only be large enough to resolve the sharp front of C for small t.

We conclude that for the case of fluctuations entering only at the top of the layer, the "visible time" should be larger in 3D than in 2D.

C. Long time limit

The instability is started earlier if the fluctuations are bigger. But how is the long-time-behavior influenced? We have addressed this question by plotting $\bar{C}$ from (57) for very long times for two different amplitudes of the porosity fluctuations γ. In the beginning, the mean concentration grows clearly faster for $F = 0.03$ than for $F = 0.003$ (Fig. 11), but the difference vanishes for large times, Fig. 12. Figure 13 presents ΔS for the two runs, which also shows no significant or systematic difference. Finally, Fig. 14 shows the contour lines of C, where the last state corresponds almost to full saturation, since C varies only between 0.88 and 1.

VIII. NUMERICAL RESULTS, FLUCTUATING PERMEABILITY

In this section we assume a constant porosity, constant boundary value for C at the top, but a fluctuating permeability $\beta \neq 0$ in space.

A. Equations and method

As basic equations we take the set (12)–(14). The flow field is now assumed to be weakly compressible. For such a case there exists no stream function and the pressure has to be computed

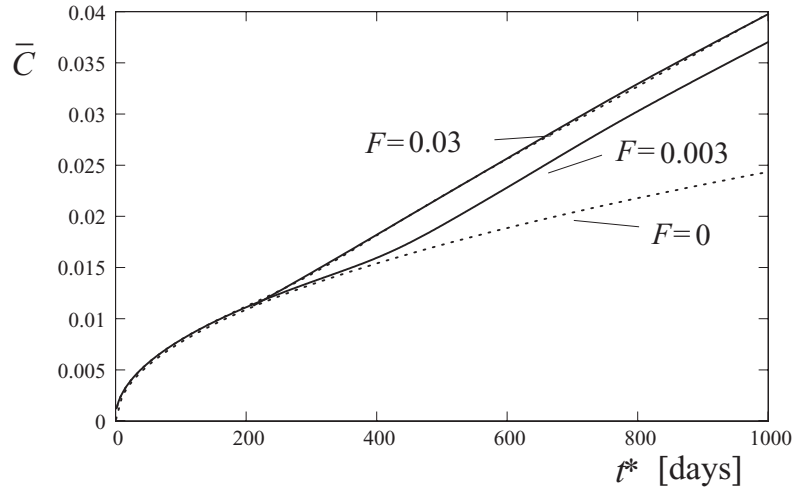

FIG. 11. Normalized mean concentration of CO_2 for the case of fluctuating porosity with different amplitudes. Also shown is the purely diffusive case when no instability is triggered ($F = 0$). Then, $\bar{C}(t) = \frac{2}{L_z}\sqrt{Dt/\pi}$.

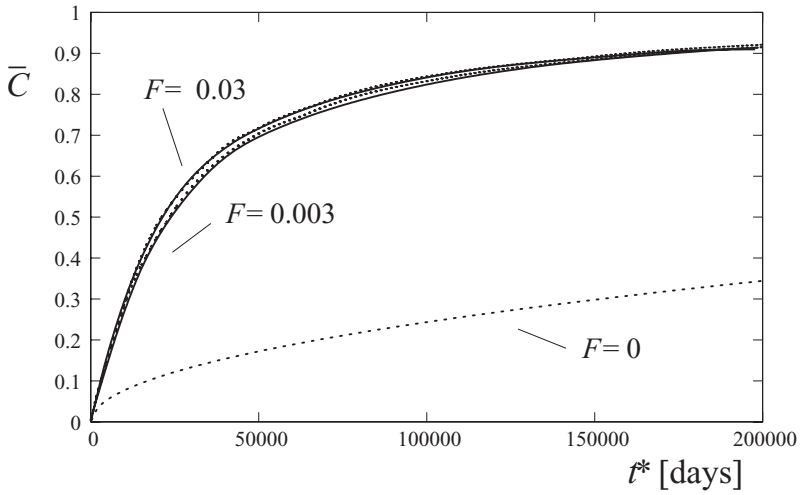

FIG. 12. Continuation of Fig. 11 for longer time where the differences vanish.

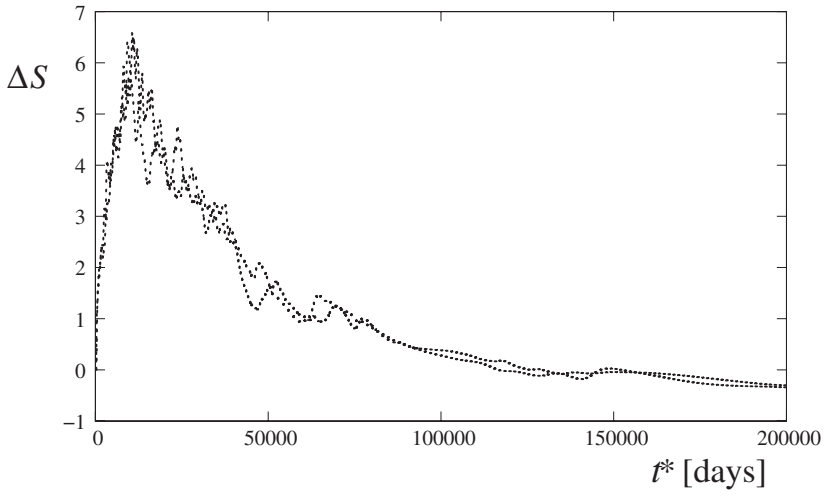

FIG. 13. Convection number for the two runs shows also no significant difference.

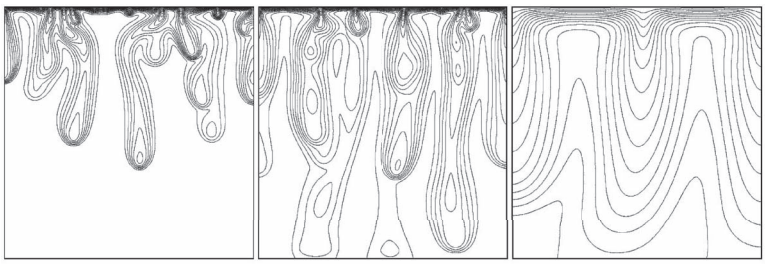

FIG. 14. Contour lines of C for the run with $F = 0.003$. The state at 200 000 days is almost saturated, the lines correspond to equally spaced values of C between 0.88 and 1.0. (a) 3000 days min/max = 0.0/1.0, (b) 6000 days min/max = 0.0/1.0, and (c) 200000 days min/max = 0.88/1.0.

explicitly by taking the divergence of (12),

$$\Delta \bar{P} = -\frac{\nabla \cdot \vec{q}}{1+\beta} + \frac{\vec{q} \cdot \nabla \beta}{(1+\beta)^2} - \partial_z C, \tag{72}$$

where $\nabla \cdot \vec{q}$ can be expressed by the concentration field C using (14). Assuming vanishing q_z on the top and on the bottom, the b.c. for the pressure

$$\partial_z \bar{P} = -C \quad \text{at} \quad z = 0,\ z_1 \tag{73}$$

can be derived from (12). Equation (72) is a Poisson equation that is inverted with the same method used for (20) and explained in Sec. III (the only difference is that we assume here periodic lateral b.c., so that the sine functions turn into plane waves). If $\bar{P}$ is known, $\vec{q}$ can be computed from (12).

If, on the other hand, we take an incompressible flow field, the first term on the rhs of (72) would be zero. Then, the laterally homogeneous concentration profile $C^0(z, t)$ with $\vec{q} = 0$ would create a pressure that depends only on z

$$\bar{P}(z, t) = -\int dz\, C^0(z, t) + \bar{P}_0,$$

which yields $\vec{q} = 0$ for all times. Thus, an inhomogeneous permeability cannot start the instability for the incompressible case.

Note that in (72) all terms are retained, so it should be valid even for large β.

B. Inhomogeneous permeability

Very often the logarithm of the permeability is normally distributed,[10]

$$\ln(K(\vec{r})/\bar{K}) = F\,\eta(\vec{r}), \tag{74}$$

where $\bar{K}$ is the geometric mean of the permeability and η a normal distribution with variance equal to one. Such a permeability has the mean value and standard deviation (lognormal distribution)

$$\langle K \rangle = \bar{K} \mathrm{e}^{F^2/2}, \qquad \sigma_K = \bar{K} \left(\mathrm{e}^{2F^2} - \mathrm{e}^{F^2} \right)^{1/2}.$$

An important measure of inhomogeneity is the coefficient of variation which can be immediately derived as

$$C_V = \frac{\sigma_K}{\langle K \rangle} = \left(\mathrm{e}^{F^2} - 1 \right)^{1/2}. \tag{75}$$

Another common measure of the variation is the Dykstra-Parsons coefficient,[11] which is related to F by

$$V_{\mathrm{DP}} = 1 - \mathrm{e}^{-F} \tag{76}$$

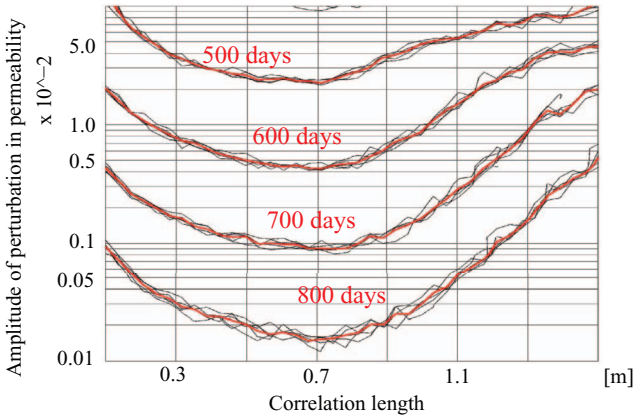

FIG. 15. One percent time, same as Fig. 7 but for fluctuations of the permeability.

and varies between zero (completely homogeneous) and one (infinitely heterogeneous). For strongly inhomogeneous rocks one has C_V of order one or larger and $V_{\mathrm{DP}} > 1/2$.

The correlation length of K is the same as that of η. Comparing (74) with (1) we may identify

$$K_0 = \bar{K}, \quad \beta(\vec{r}) = \exp(F\,\eta(\vec{r})) - 1. \tag{77}$$

To compare the onset time by inhomogeneous permeability, we start with the case where $F \ll 1$. Then we may expand (75)–(77) and find

$$\beta \approx F\eta, \qquad C_V \approx V_{\mathrm{DP}} \approx F.$$

Figure 15 shows the one percent times for several values of F and the correlation length. It turns out that for comparable perturbation amplitudes the times are much larger than for the case of fluctuating porosity or boundary concentration. Thus the diffusive state seems to be more stable against disturbances originating from permeability fluctuations only. This can be explained by the fact that the compressibility of the fluid is very small (a factor $\alpha C_0 \approx 0.01$ in (72)) and it takes much larger values for β to create a significant flow field to start the instability. A similar influence between fluctuating permeability and porosity on onset times is reported in Ref. 7.

C. Long time limit

To conclude this section we present two runs showing pattern formation in the long time limit for strongly heterogeneous porous media with $C_V > 1/2$. For the first run, we take a rather large correlation length and $F = 0.5$,

$$\ell = 1.5\ \mathrm{m}, \quad F = 0.5, \quad \langle K\rangle = 1.13\,\bar{K}, \quad V_{\mathrm{DP}} = 0.4, \quad C_V = 0.53,$$

for the second we take a small ℓ and $F = 0.7$,

$$\ell = 0.2\ \mathrm{m}, \quad F = 0.7, \quad \langle K\rangle = 1.28\,\bar{K}, \quad V_{\mathrm{DP}} = 0.5, \quad C_V = 0.8.$$

In both runs, the distribution of K deviates strongly from a Gaussian, as shown in Fig. 16. As typical for a lognormal distribution, it is more likely to find smaller values of K, but on the other hand, due to the exponential in (77) K can become very large in few rare places, forming a kind of channels. This is especially important for larger correlation lengths (time series in Fig. 17 at top) whereas for small ℓ the channels are too thin and disconnected, so they cannot contribute to CO_2 transport (Fig. 17, bottom). In the early stages in Fig. 17 at top, it can be seen that finger formation and growth occurs mainly in the domains where K is large. The fingers fall down not only vertically as it is the case for a homogeneous medium but also show motion in the horizontal direction, influenced by the channels.

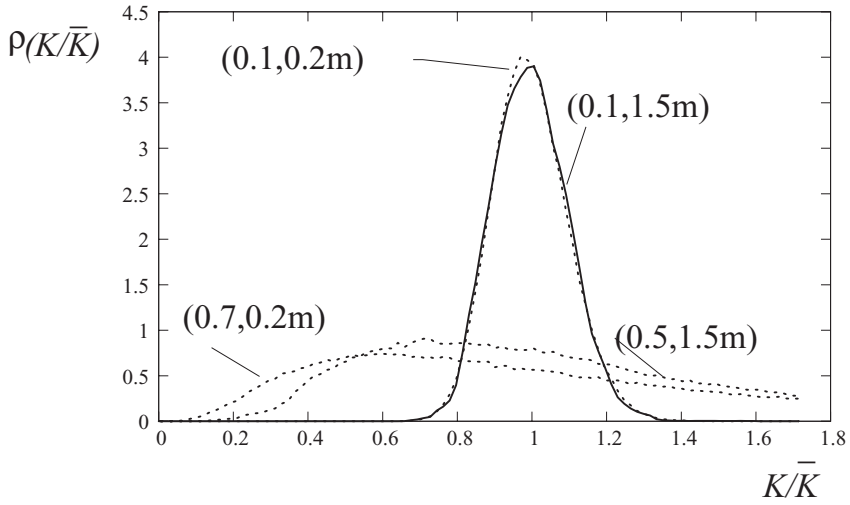

FIG. 16. Distribution of K for several values of amplitude and correlation length (F, ℓ). For small amplitudes, the distribution is almost Gaussian, where it deviates strongly for larger F.

Figure 18 shows ΔS versus time. From the left frame it is remarkable that temporal fluctuations seems to be rather strong now, at least for the larger correlation length. The right frame shows the earlier stages. Convection sets in already after about 100 days. The larger amplitude $F = 0.7$ shows a behavior similar to the simple model of Sec. V, Fig. 4. The onset is not sharp but rather starts smoothly from the beginning.

IX. NUMERICAL RESULTS INCLUDING THERMAL GRADIENTS

A natural vertical temperature gradient of the size of 0.025 K/m or larger, the geothermal gradient, exists across an aquifer in the vertical direction.[37] Temperature increases with depth and if the density of the water is assumed to depend linearly on temperature, buoyancy should destabilize the motionless state if the condition

$$R_T \geq 4\pi^2 \tag{78}$$

is fulfilled.[38] Here, R_T is the (thermal) Rayleigh number

$$R_T = \frac{K_0 g \gamma_T \rho_0 L_z^2 \beta_T}{\mu\kappa} \tag{79}$$

with the thermal expansion coefficient

$$\gamma_T = -\frac{1}{\rho_0}\frac{\partial \rho^*}{\partial T^*}\bigg|_{T_0} \qquad \rho_0 = \rho^*(T_0),$$

the thermal diffusivity κ and the geothermal gradient β_T. Taking the parameters from above and $\gamma_T = 0.0004\ \mathrm{K}^{-1}$, $\beta_T = 0.05$ K/m,[39] one finds that a layer thicker than $L_z^c \approx 300$ m would be thermally unstable and convection rolls (Rayleigh-Bénard convection) would be formed.[40] However, it turns out that the motion due to thermal gradients is much less than that due to concentration and can therefore be safely neglected, even for rather thick layers where the motionless fluid would be thermally unstable. Note that due to the increase in pressure at higher depths the decrease in density from temperature increase will be even less pronounced, leading to a smaller effective γ_T.

If, on the other hand, *horizontal* thermal gradients exist, buoyancy cannot be compensated by a hydrostatic pressure and the fluid would always move, no matter how small the temperature gradient is.[41,42]

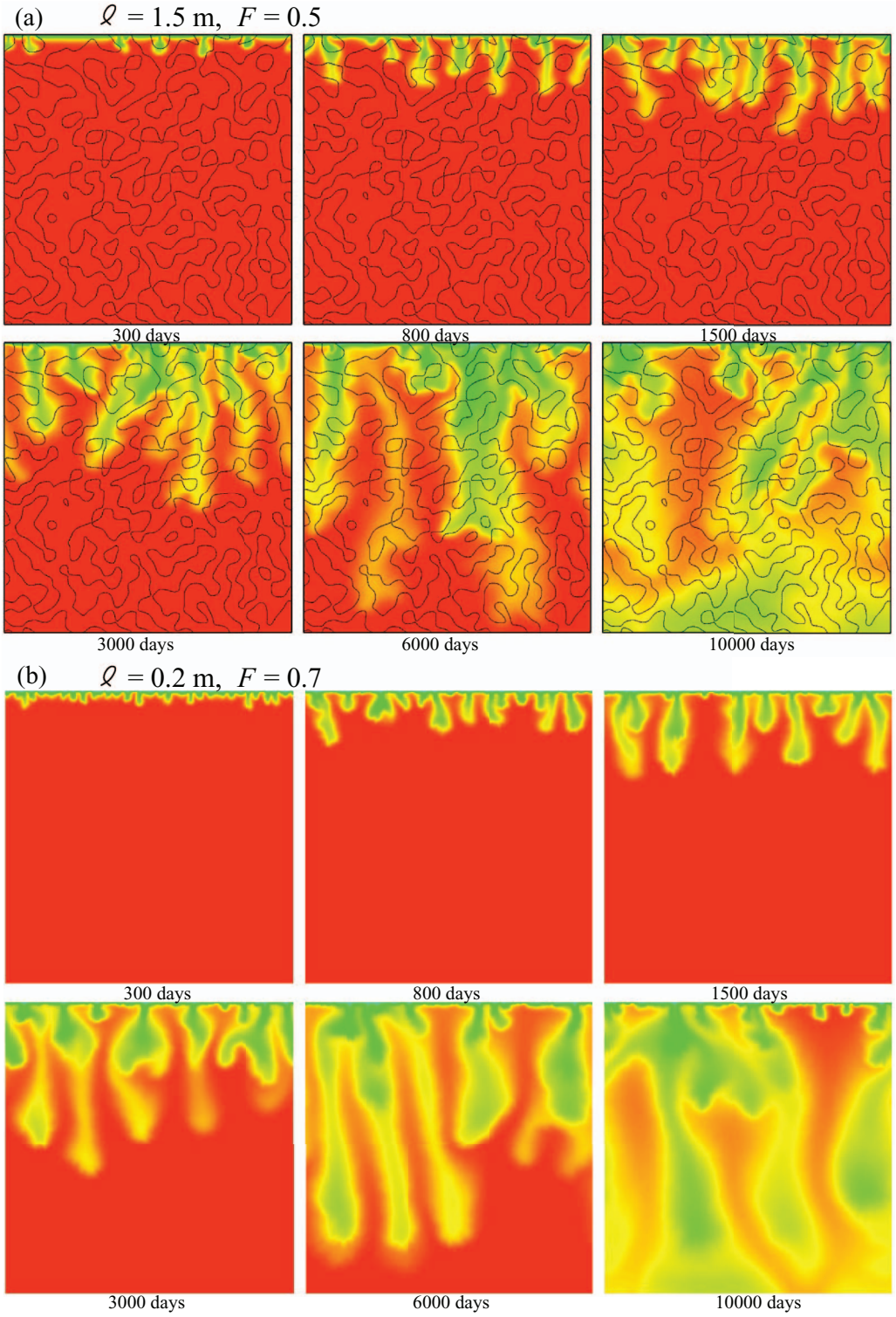

FIG. 17. (a) Time series of CO_2 concentration for large correlation length and amplitude. Channeling can be seen in the early stages. Contour lines show the location of $K = \bar{K}$. (b) Time series for smaller correlation length.

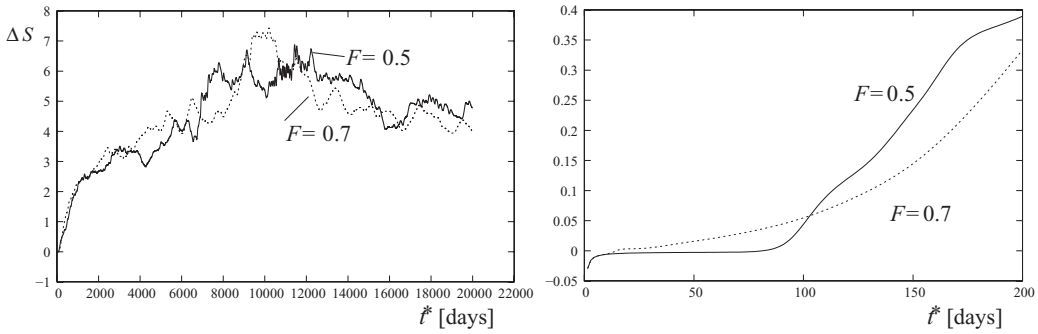

FIG. 18. Left frame: Behavior of ΔS for longer times. Temporal fluctuations are more pronounced than for the case of fluctuating porosity, compare to Fig. 13. Right frame: Early stage shows a kind of imperfect bifurcation for $F = 0.7$.

In this section, we assume a prescribed temperature field that has a horizontal space dependence,

$$\partial_{x^*} T^* \neq 0.$$

Such a dependence may origin from inhomogeneous thermal conductivities of the rock and can have a value of a few degrees per 1000 m.

A. Boussinesq approximation

First we introduce a dimensionless temperature by scaling the temperature with the total temperature difference on L_z according to

$$T^* = \beta_T \, L_z \, T.$$

If we take the Boussinesq approximation and ignore all other fluctuations, the problem considered in 2D is extended to

$$\Delta\Phi = \partial_x C + H \partial_x T, \tag{80}$$

$$\partial_t C = -\partial_z \Phi \partial_x C - \partial_x \Phi \partial_z C + \Delta C, \tag{81}$$

where H is a heat parameter

$$H = \frac{\gamma_T \beta_T L_z}{C_0 \alpha} = \frac{R_T}{R} \, L, \tag{82}$$

with the Lewis number $L = \kappa/(n_0 D)$. For a pure fluid, only (80) remains taking the simple form

$$\Delta\Phi = H \partial_x T. \tag{83}$$

B. Constant horizontal temperature gradient

From (83) we may determine the flow field for any given temperature distribution. If we assume a circular region with radius R and a constant temperature gradient $\partial_x T = \delta T/R$, a solution to (83) would read $\Phi = \dfrac{H \delta T}{4R}(x^2 + z^2)$. We can then estimate the maximal velocity after re-scaling to

$$q^*_{\max} = \frac{K_0 g \rho_0 \gamma_T}{2\mu} \delta T^*,$$

which would yield for our parameters a value of 10^{-11} to 10^{-10} m/s, less than one millimeter per year.

Despite this very small value, this motion can trigger the convective instability. Figure 19 shows the streamlines of the first phase of such a case where no further perturbations are added

FIG. 19. Stream lines of the velocity field, numerical solution of (80) and (81) for a constant lateral temperature gradient of 1 K/km. Only the upper half of the layer is shown. (a) 10 days, (b) 600 days, and (c) 1100 days.

($\beta = \gamma = 0$). In Fig. 19(a), only the base state (upper half shown) is visible which consists of a very slowly turning roll. After about 600 days, small scale vortices become visible at the corners. Here, fluid motion is mainly in vertical direction which leads to an increase/decrease of the local velocity of the CO_2-diffusion front and as a consequence to a horizontal inhomogeneity which then may start the instability. In Fig. 19(c), small scale motion is clearly dominating the primary thermal motion by a factor 1000. Figure 20 shows ΔS defined in (59), in Fig. 21 the maximal velocity value $|\vec{q}|$ is plotted. It can be clearly seen that the instability occurs after about 220 days, rather independent from the size of the thermal gradient.

C. Inhomogeneous thermal conductivity

The thermal conductivity of the rocks may vary in space, depending on their composition. This variation can produce a horizontal thermal gradient which is normally much smaller than the vertical one.

To compute the stationary temperature field for a given thermal conductivity $\lambda_T(x, z)$, one finds a solution of the energy equation

$$\nabla \cdot [\lambda_T(x, z)\nabla T(x, z)] = 0 \tag{84}$$

in the domain $0 \le x \le x_1, 0 \le z \le z_1$. The boundary conditions are

$$T(x, 0) = T_0, \quad T(x, z_1) = T_0 - z_1, \quad T(0, z) = T(x_1, z) = T_0 - z.$$

To solve (84) numerically, we first write it in the form

$$\lambda_T \Delta T + (\nabla \lambda_T) \cdot (\nabla T) = 0 \tag{85}$$

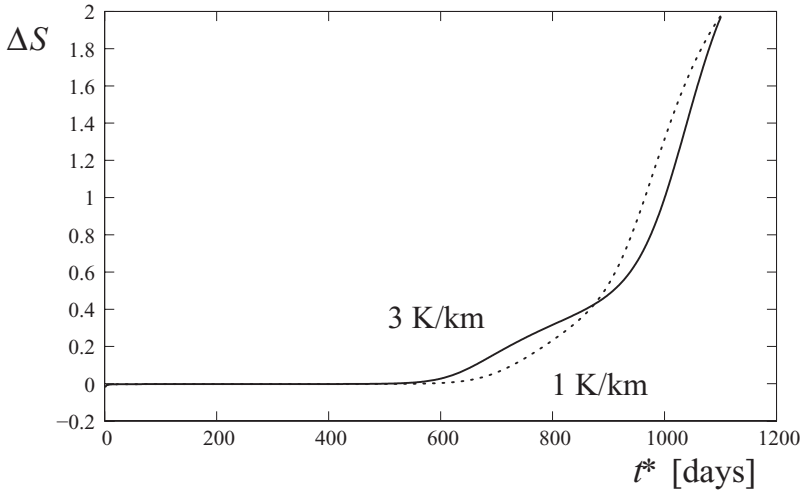

FIG. 20. Convection number if the instability is started only by a lateral temperature gradient of 1 K/km (dotted) and 3 K/km (solid).

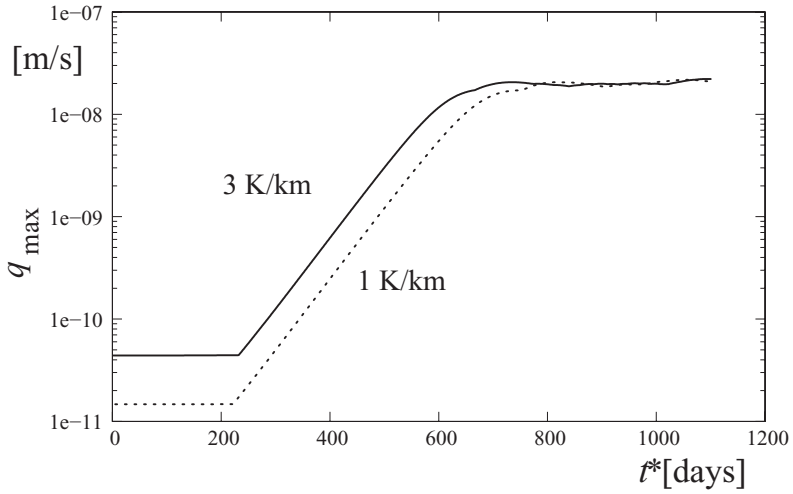

FIG. 21. Maximal velocity in the domain for the two constant lateral temperature gradients.

and use a Gauss-Seidel algorithm[19] on a rectangular finite difference mesh which yields an iteration formula

$$T_{ij}^{(n+1)} = \frac{1}{2}\frac{1}{\Delta x^2+\Delta z^2}\Big\{\Delta z^2\left(1+\frac{1}{4}\lambda_{ij}^{(x)}\right)T_{i+1,j}^{(n)} + \Delta z^2\left(1-\frac{1}{4}\lambda_{ij}^{(x)}\right)T_{i-1,j}^{(n)} + \Delta x^2\left(1+\frac{1}{4}\lambda_{ij}^{(z)}\right)T_{i,j+1}^{(n)} + \Delta x^2\left(1-\frac{1}{4}\lambda_{ij}^{(z)}\right)T_{i,j-1}^{(n)}\Big\}, \tag{86}$$

where $i = 2\ldots M-1, j = 2\ldots N-1$ and $\Delta x = x_1/(M-1)$, $\Delta z = z_1/(N-1)$. The abbreviations are

$$\lambda_{ij}^{(x)} = \frac{\lambda_{i+1,j}-\lambda_{i-1,j}}{\lambda_{ij}}, \qquad \lambda_{ij}^{(z)} = \frac{\lambda_{i,j+1}-\lambda_{i,j-1}}{\lambda_{ij}}$$

with T_{ij}, λ_{ij} being the value of T and λ_T, respectively, at the grid point (i, j). The iteration is started with

$$T_{ij}^{(0)} = T_0 - (j-1)\Delta z$$

and stopped when the absolute error

$$E = \beta_T L_z \sum_{ij}\left|T_{ij}^{(n)} - T_{ij}^{(n-1)}\right|$$

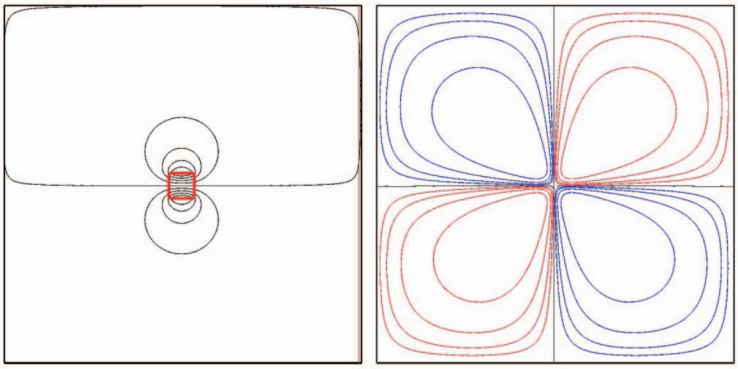

FIG. 22. Quadratic enclave of higher thermal conductivity. Left: temperature difference to the linear state, right: stream function of the velocity field caused by buoyancy.

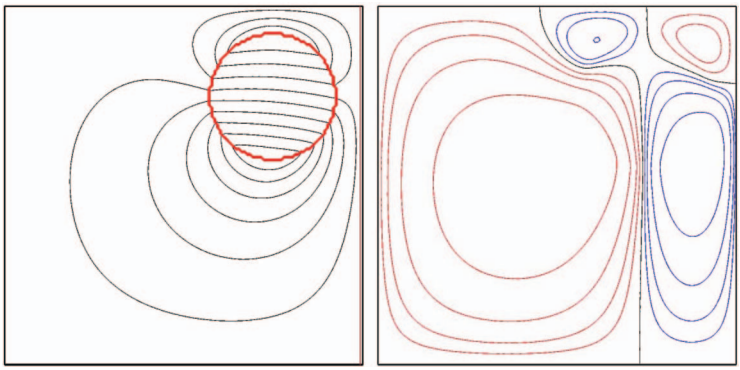

FIG. 23. Same as in Fig. 22 but for a circular enclave near the top of the domain.

falls below 10^{-6} K, which is the case after 5000–10 000 iterations. The domain size is chosen with $L_x = L_z = 100$ m, for discretization, a mesh with 128×128 grid points is used.

Figure 22, left frame, shows the temperature field of a quadratic enclave in the middle of the domain, where the conductivity is 10% larger than for the rest of the rock. The contour lines denote the difference from the linear state,

$$\delta T = T(x, z) - T_0 + z.$$

The right frame shows the corresponding velocity field due to buoyancy, found by integrating (83). In Fig. 23 we take a circular enclave close to the top, whereas in Fig. 24 1D-discontinuity in form of a sinusoidal interface is used. The two regions separated by the interface differ in their thermal conductivities by 10%.

For the circular enclave we find the maximal horizontal temperature gradient of about 2.6 K/km, compared to the discontinuity, where it is everywhere less than 1 K/km. For all cases, $\beta_T = 0.05$ K/m and the variation of λ_T is 10%. Note that the horizontal gradients depend linearly on the geothermal gradient, so for smaller β_T they are accordingly smaller.

D. Instabilities induced by inhomogeneous thermal gradients

Finally, we take the temperature distributions shown in Figs. 22–24 as input for (80) and (81), and study the onset of instability when no further perturbations exist. The domain size is $L_x = L_z = 100$ m, but all other parameters are kept unchanged. Figure 25 compares the stream lines for the three different temperature fields at the same time at 1200 days. One can see a reminiscence of the patterns to their corresponding temperature distributions. For the enclaves, finger formation starts

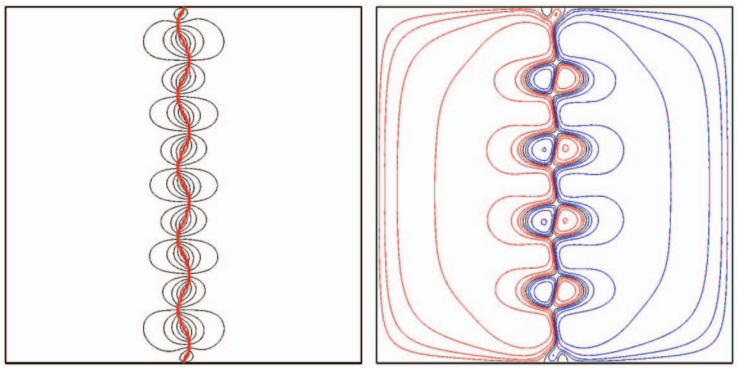

FIG. 24. A sinusoidal discontinuity between domains of different thermal conductivities can give rise to a rather complicated temperature and velocity field.

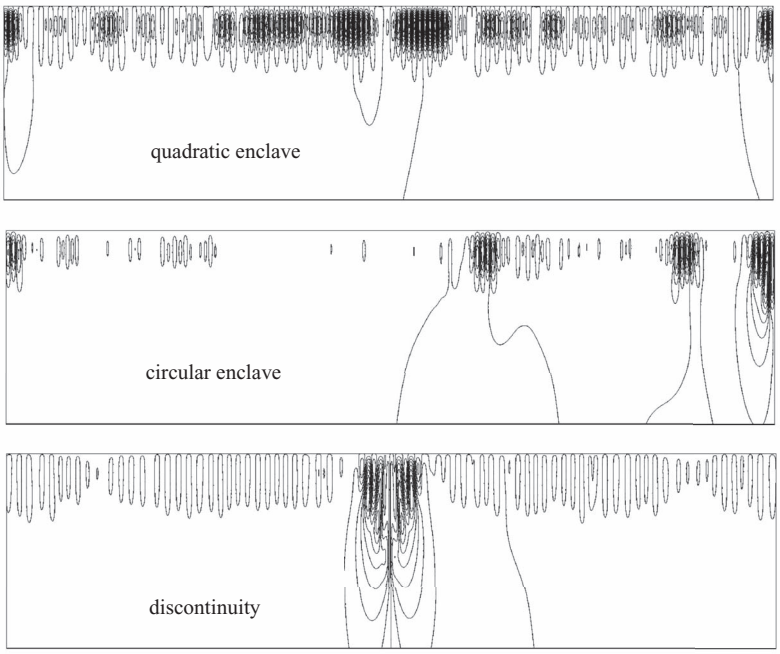

FIG. 25. Streamlines of the velocity field at 1200 days, numerical solution of (80) and (81) for temperature gradients that origin from inhomogeneous thermal conductivities. The side length and height are 100 m, but only the upper 5 m is plotted.

mainly near the inhomogeneous zones and at the corners, whereas for the discontinuity, the velocity is rather large at the discontinuity from where it spreads out laterally. Although the absolute value of the lateral temperature gradient is the smallest one for the discontinuity, this configuration leads to the fastest growth and earliest onset of convection, which can be seen from Figs. 26 and 27, where we compare the values of the convection number and $q_{\max}$ as a function of time.

X. DISCUSSION IN RELATION TO EARLIER WORK

The main purpose of our work is to study onset and the early phase of convection of a buoyancy-driven water-CO_2 mixture in porous media. Due to the time and space dependent basic state, the linear stability problem is not standard and there exist different definitions of the onset time (that

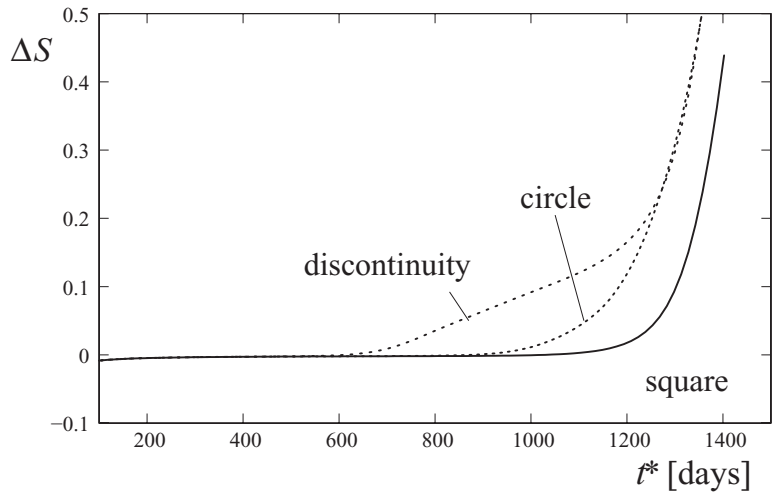

FIG. 26. ΔS for the three runs of Fig. 25.

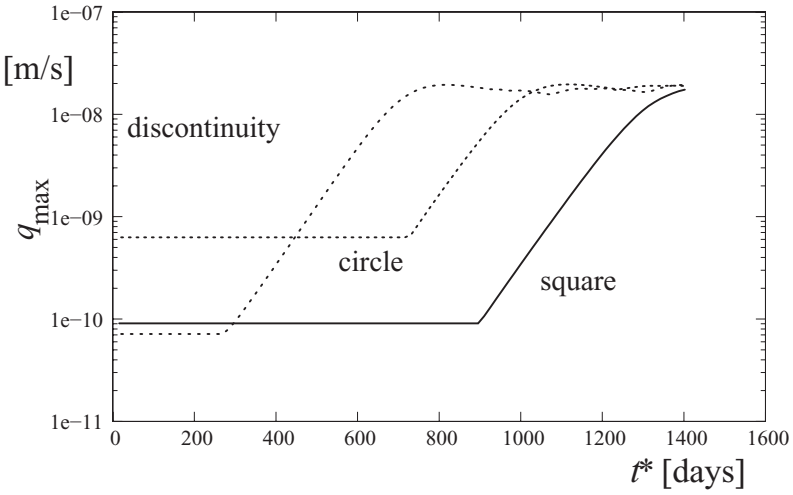

FIG. 27. Maximal velocity for the three runs.

is, the critical time) where the base state loses stability. Table II summarizes the results of our work together with results from the literature. The different scalings and material parameters used in the literature make it difficult to compare our work directly with previous studies. For a clear comparison we express all times found from the literature in dimensionless units that have to be multiplied by

$$\tau = \left(\frac{n_0 \mu}{K_0 g \rho_0 \alpha C_0} \right)^2 D \tag{87}$$

to obtain times in seconds (scaling (8) and (9)). Where necessary, τ is specified in the table.

The differences of the linear times are due to the different methods: some authors use frozen-time analysis,[27] others consider an amplification factor (35)[4] or take the minimum of the mean square disturbances of the concentration field.[6,9,43] For the last method, the initial conditions of the disturbances are important. In Ref. 3, the dominant mode solution is applied which yields a much larger onset time.

The times at which convective patterns become visible may differ over a wide range with direct numerical solutions of the fully nonlinear problem. On one hand, they depend on the definition of "visible" time. Usually, this is defined as the moment where the CO_2 flux by convection and diffusion differs by a certain amount, say one percent, from that by diffusion alone. We adopt this definition in our work. The other point is the size and length scale of the initial perturbations and/or of perturbations during the evolution process caused by inhomogeneous material properties. Here we place the emphasis on spatially varying permeability and porosity.

TABLE II. Onset time (first column) and "visible" time in units of τ, (87). Regions specified in the first row are based on the variations of amplitude and length scale of the perturbations, shown in Figs. 7, 9, and 15.

	Linear	Porosity	Concentration	Permeability	Thermal	τ
This work	50[a]	450–3600	220–3000	1800–4500	3000–6000	0.2 days
Rapaka[4]			300			18.5 days
Slim[6]	48					
Pau[7]		1600		3600		62 s
Riaz[3]	146					
Farajzadeh[8]				2000		[b]
Xu[9]	75					
Ennis-King[43]	75					

[a]From Fig. 3, frozen-time analysis.
[b]Domain depth and diffusion coefficient not provided.

All the "visible" times are much larger than the onset times from the linear methods. One exception is Ref. 4, where the time is not clearly stated and we determine it from their Fig. 6. We could not find the amplitude of the initial condition, which is the one that yields the fastest linear growth. This optimal initial condition together with a presumably rather large amplitude could lead to such a relatively short time.

Another even shorter one percent time of $t \approx 141$–177 ($\tau \approx 28$ s) is stated in recent laboratory experiments.[44] Here the authors are not sure about size and nature of perturbations that finally destabilize the base state.

For our results based on thermal initial fluctuations there may be no reported work in the literature.

XI. CONCLUSIONS

Various authors use different definitions of the critical time (or onset time). These definitions include the time when

(i) the frozen-time diffusive base state (23) becomes unstable,
(ii) perturbations of the time-dependent base state start to grow,
(iii) the amplification factor (35) begins to grow,
(iv) the amplification factor (35) reaches unity.

All these definitions lead to different times, see Sec. IV D. Taking (ii), the critical time may also depend on the form of the perturbations. All critical times have the common feature they are small compared to the time where convection manifests itself in visible deviations of the concentration from the diffusive base state.

Apart from (i)–(iv) we use a different characteristic time in our paper, called visible time or one-percent time as defined above.

The visible time can be considerably longer than the critical times and has more practical relevance. It also depends on the type, magnitude, and length scale of the perturbations of the horizontally homogeneous diffusive base state. The investigation of these relationships is the purpose of our work. We use different sources for perturbations: fluctuations of the concentration field, of permeability and porosity as they are observed in natural rocks. Concentration fluctuations are assumed to be present only on the top surface of the domain. Their propagation by diffusion in the bulk is examined in Sec. VII B 2 where it turns out that the spatial domain dimensionality is important. For the case of fluctuating permeability, the flow field has to be compressible as shown in Sec. VIII. Finally, thermal fluctuations from horizontal inhomogeneities in the thermal conduction are studied in Sec. IX. It is shown that they may have the same effect and influence on the visible times the rock inhomogeneity or concentration fields.

As a concluding remark we may point out that the two times, onset (linear) and "visibility" (nonlinear) differ by a factor 10 to 100, depending on the origin of perturbations, but even more on their size and scale. Since early onset and large convection is desirable for carbon dioxide storage, these results could be important for site selection.

ACKNOWLEDGMENTS

This work was supported by member companies of the Reservoir Engineering Research Institute (RERI). M.B. acknowledges financial support and great hospitality from RERI during a research stay in Palo Alto.

[1] A. Firoozabadi and P. Cheng, "Prospects for subsurface CO_2 sequestration," AIChE J. **56**, 1398 (2010).
[2] M. C. Cross and P. C. Hohenberg, "Pattern formation outside equilibrium," Rev. Mod. Phys. **65**, 851 (1993).
[3] A. Riaz, M. Hesse, H. A. Tchelepi, and F. M. Orr, Jr., "Onset of convection in a gravitationally unstable diffusive boundary layer in porous media," J. Fluid Mech. **548**, 87 (2006).
[4] S. Rapaka, S. Chen, R. J. Pawar, P. H. Stauffer, and D. Zhang, "Non-modal growth of perturbations in density-driven convection in porous media," J. Fluid Mech. **609**, 285 (2008).

[5] P. Cheng, M. Bestehorn, and A. Firoozabadi, "Effect of permeability anisotropy on density-driven flow for CO_2 sequestration in saline aquifers," Water Resour. Res. **48**, W09539, doi:10.1029/2012WR011939 (2012).
[6] A. C. Slim and T. S. Ramakrishnan, "Onset and cessation of time-dependent, dissolution-driven convection in porous media," Phys. Fluids **22**, 124103 (2010).
[7] G. S. H. Pau, J. B. Bell, K. Pruess, A. S. Almgren, M. J. Lijewski, and K. Zhang, "High-resolution simulation and characterization of density-driven flow in CO_2 storage in saline aquifers," Adv. Water Resour. **33**, 443 (2010).
[8] R. Farajzadeh, P. Ranganathan, P. L. J. Zitha, and J. Bruining, "The effect of heterogeneity on the character of density-driven natural convection of CO_2 overlying a brine layer," Adv. Water Resour. **34**, 327 (2011).
[9] X. Xu, S. Chen, and D. Zhang, "Convective stability analysis of the long-term storage of carbon dioxide in deep saline aquifers," Adv. Water Resour. **29**, 397 (2006).
[10] J. L. Jensen, L. W. Lake, P. W. M. Corbett, and D. J. Goggin, *Statistics for Petroleum Engineers and Geoscientists (Handbook of Petroleum Exploration and Production)* (Elsevier, Amsterdam, 2000).
[11] H. Dykstra and R. L. Parsons, "The prediction of oil recovery by waterflood," in *Secondary Recovery of Oil in the United States* (American Petroleum Institute, New York, 1950), p. 160.
[12] E. Lindeberg and D. Wessel-Berg, "Vertical convection in an aquifer column under a gas cap of CO_2," Energy Convers. Manage. **38**, S229 (1997).
[13] J. Bear and Y. Bachmat, *Introduction to Modeling of Transport Phenomena in Porous Media* (Kluwer, Dordrecht, 1990).
[14] D. V. Ellis and J. M. Singer, *Well Logging for Earth Scientists* (Springer, 2007).
[15] Z. Li and A. Firoozabadi, "Cubic-plus-association equation of state for water-containing mixtures: Is cross association necessary?," AIChE J. **55**, 1803 (2009).
[16] S. Chandrasekhar, *Hydrodynamic and Hydromagnetic Stability* (Dover, New York, 1981).
[17] E. W. Lemmon, M. O. McLinden, and D. G. Friend, "Thermophysical properties of fluid systems," in *NIST Chemistry WebBook* (NIST, 2012), Vol. 69.
[18] J. Mutoru, A. Leahy-Dios, and A. Firoozabadi, "Modeling infinite dilution and Fickian diffusion coefficients of carbon dioxide in water," AIChE J. **57**, 1617 (2011).
[19] C. A. J. Fletcher, *Computational Techniques for Fluid Dynamics* (Springer, Berlin, 1988), Vol. I.
[20] R. A. Gentry, R. E. Martin, and B. J. Daly, "An Eulerian differencing method for unsteady compressible flow problems," J. Comput. Phys. **1**, 87 (1966).
[21] P. J. Roache, *Computational Fluid Dynamics* (Hermosa, 1976).
[22] P. N. Swarztrauber, "Vectorizing the FFTs," in *Parallel Computations* (Academic, 1982), pp. 51–83.
[23] W. H. Press, S. A. Teukolsky, W. T. Vetterling, and B. P. Flannery, *Numerical Recipes: The Art of Scientific Computing*, 3rd ed. (Cambridge University Press, 2007).
[24] M. Bestehorn, "Phase and amplitude instabilities for Bénard-Marangoni convection in fluid layers with large aspect ratio," Phys. Rev. E **48**, 3622 (1993).
[25] D. H. Sharp, "An overview of Rayleigh-Taylor instability," Physica D **12**, 3 (1984).
[26] M. Abramowitz and I. A. Stegun, *Handbook of Mathematical Functions* (Dover, New York, 1972).
[27] C. T. Tan and G. M. Homsy, "Stability of miscible displacement in porous media-rectilinear flow," Phys. Fluids **29**, 3549 (1986).
[28] K. Ghesmat, H. Hassanzadeh, and J. Abedi, "The impact of geochemistry on convective mixing in a gravitationally unstable diffusive boundary layer in porous media," J. Fluid Mech. **673**, 480 (2011).
[29] J. R. Tredicce, G. L. Lippi, P. Mandel, B. Charasse, A. Chevalier, and B. Picque, "Critical slowing down at a bifurcation," Am. J. Phys. **72**, 799 (2004).
[30] M. C. Torrent and M. San Miguel, "Stochastic-dynamics characterization of delayed laser threshold instability with swept control parameter," Phys. Rev. A **38**, 245 (1988).
[31] J. R. Waggoner, J. L. Castillo, and L. W. Lake, "Simulation of EOR processes in stochastically generated permeable media," SPE Form Eval. **7**, 173 (1992).
[32] A. Montoglou and J. L. Wilson, "The turning bands method for simulation of random fields using line generation by spectral method," Water Resour. Res. **18**, 1379, doi:10.1029/WR018i005p01379 (1982).
[33] F. J. Molz, H. Rajaram, and S. Lu, "Stochastic fractal-based models of heterogeneity in subsurface hydrology," Rev. Geophys. **42**, RG1002, doi:10.1029/2003RG000126 (2004).
[34] C. W. Gardiner, *Handbook of Stochastic Methods* (Springer, Berlin, 1983).
[35] P. E. Greenwood and M. S. Nikulin, *A Guide to Chi-Squared Testing* (Wiley, 1996).
[36] F. H. Busse, "Transition to turbulence in Rayleigh-Benard convection," Top. Appl. Phys. **45**, 97 (1985).
[37] H. Nasrabadi, A. Firoozabadi, R. Oliveira, and A. J. M. Vieira, "Interpretation of an unusual bubblepoint pressure variation in an offshore field," SPE 113574 (2008).
[38] J. W. Elder, "The unstable thermal interface," J. Fluid Mech. **32**, 69 (1968).
[39] K. G. O. Petrobras, "Nonisothermal gravitational equilibrium model," SPE Reservoir Eval. Eng. **2**, 211 (1999).
[40] M. Bestehorn, "Fluid dynamics and pattern formation," in contribution to *Encyclopedia of Complexity and System Science*, edited by R. A. Meyers (Springer, Berlin, 2009), pp. 3611–3641.
[41] K. Ghorayeb and A. Firoozabadi, "Modeling multicomponent diffusion and convection and in porous media," SPE J. **158**, 12 (2000).
[42] K. Ghorayeb and A. Firoozabadi, "Numerical study of natural convection and diffusion in fractured porous media," SPE J. **5**, 12 (2000).
[43] J. Ennis-King, I. Preston, and L. Paterson, "Onset of convection in anisotropic porous media subject to a rapid change in boundary conditions," Phys. Fluids **17**, 084107 (2005).
[44] T. J. Kneafsey and K. Pruess, "Laboratory experiments and numerical simulation studies of convectively enhanced carbon dioxide dissolution," Energy Procedia **4**, 5114 (2011).